Supporting Information

Anomalous self-reduction of layered double hydroxide (LDH): from α-$Ni(OH)_2$ to hexagonal close packing (HCP) Ni/NiO by annealing without reductant

X. Ge, C. D. Gu[1], X.L. Wang, J.P. Tu

State Key Laboratory of Silicon Materials, Key Laboratory of Advanced Materials and Applications for Batteries of Zhejiang Province and Department of Materials Science and Engineering, Zhejiang University, Hangzhou 310027, China.

The following informations are provided to give detailed decscription of the experiment and to support the mechanism of self-reduction that we proposed.

Figure S1-S3: **TG, UV-Vis, FTIR** and **XPS** for 10C-S Ni LDH and 50W Ni LDH

Figure S4 and S5: **^{1}H NMR** and **FTIR** of CU before/after thermal decomposition

Figure S6-S9: **electrochemical measurements** of 10C-S A-Ni and 50W Ni LDH

Table S1-S5: **IC, ICP** and **CNH** analysis of 10C-S Ni LDH and 50W Ni LDH

[1] *Corresponding Author
Tel./fax.: +86 571 87952573
E-mail addresses: cdgu@zju.edu.cn; changdong_gu@hotmail.com (C. D. Gu)

Experimental details

1. Preparation of deep eutectic solvent and its solution containing Ni^{2+} ions.

ChCl (AR, Aladdin) was dried at 70 °C for 24 h before used. Urea (AR, Aladdin) was used as received. The ChCl/urea mixture-based deep eutectic solvent (DES) was formed by stirring the two components in a molar ratio of 1 ChCl:2 urea at 80 ºC, until a homogeneous colorless liquid was formed.[1] During heating and storage, the container was covered by an air proof plastic film. The ChCl/urea mixture-based ionic liquid will be hereafter denoted as "CU" for convenience. Then, an appropriate amount of $NiCl_2$•$6H_2O$ was dissovled in CU at 50 °C under magnetic stirring to form a solution containing 0.1 M Ni^{2+}. The water content of the final solution was determined to be about 20000 ppm by Karl–Fischer titration (Zhibo Zhenggong titrators WS-3).

2. Preparation of Ni LDH and A-Ni

The preparation of Ni LDH is based on modifying a hot-injection technique we previously developed.[2] As-purchased $NiCl_2 \cdot 6H_2O$ was dissolved into CU to get a 0.1 M $NiCl_2$:CU solution. 50 mL 0.1 M $NiCl_2$:CU solution was transferred into a three-neck flask. A heater was preheated and stabilized at 190 °C. Then the flask containing solution was put into the heater and stirred at 500 r/min magnetically. After 40 min, the temperature of the solution rose from room temperature to 150±5 °C. The speed of the magneton was then accelerated to 750 r/min. Then a given amount of solution containing OCN^- ion (0.1 g mL^{-1} NaOCN in water) or pure water was injected at different speed. 30 seconds later, the flask was taken out and put into an ice bath for rapid cooling while keeping stirring.

The cooled solution was diluted with 50 mL methanol and centrifuged. The precipitate was then washed with methanol for twice and ethanol for once, centrifuged and dried at 70 ^{o}C for 8h. The obtained LDH precursors are denoted according to the method used in the water (or NaOCN solution) injection step. Two samples denoted as 10C-S LDH and 50W LDH are given in this paper. The number means the volume of water (or NaOCN solution) injected. The character "C" or "W" shows what kind of solution is injected ("C" stands for cyanate solution and "W" stands for water). "S" means slow (10 mL OCN^- solution was added gradually in 10 minutes). For the 50W LDH sample, the injection was also completed rapidly in less than 5 seconds.

We present 50W Ni LDH instead of 10W Ni LDH because it can better represent the structure of samples obtained in water-rich condition.

The annealed nickel compounds (A-Ni) were obtained by simply annealing the Ni LDH precursors under Ar atmosphere at 300 ^{o}C (heating rate at 10 ^{o}C min^{-1}) for 4h in a tube furnace. The annealed products are denoted as 10C-S A-Ni, and 50W A-Ni, according to the precursor used.

3. Material characterization

Structure and morphology of the obtained materials were characterized by X-ray diffraction (XRD, RigakuD/Max-3B), X-ray photoelectron spectroscopy (XPS, AXIS UTL-TRADLD), scanning electron microscope (SEM, Hitachi S-4800), and transmission electron microscope (TEM, JEM 200CX at 160 kV, Tecnai G2 F20 at 200 kV). UV-Vis spectra were recorded using UV-3600

(SHIMADZU, Japan). The thermal decomposition behavior of the nickel LDH precursors was tested by Thermo-gravimetric (TG) using a TA Q600 instrument in a temperature range from 20 to 600 ^{o}C with a heating rate of 10 ^{o}C min^{-1} under Ar protection. FTIR spectra were obtained by Nicolet5700 (ThermoFisher Co.). The magnetic properties were measured on a Quantum Design MPMS-5 SQUID magnetometer.

The details about the characterization of chemical stoichiometry of nickel LDH and solvent property are given in the Supporting Information. Briefly, the element content of the nickel LDH was determined by inductively coupled plasma atomic emission spectroscopy (ICP-AES, IRIS Intrepid II XSP), Ion chromatography (IC, DIONEX ics-2000), and elemental analyzer (Flash EA 1112, ThermoFinnigan). The property of the solvent after thermal decomposition was characterized with FTIR and ^{1}H NMR (DMX-500, BRUKER).

4. Characterization of the thermal decomposition of CU

In order to understand the distinct solvent effect, NMR and FTIR were taken to investigate the property of the CU solvent before and after heating. For 1H NMR test, the heated/unheated CU sample was first dispersed in deuterated chloroform ($CDCl_3$). The heating condition is similar to that used in the sample preparation of Ni LDH. A heater was preheated and maintained at a given temperature. Then a flask containing 50 mL CU solvent was put into the heater. The solvent was magnetically stirred at 500 r/min. 40 min later, the temperature of the solvent reached 150 or 210 ^{o}C, depending on

the temperature of the preheated heater. Then the flask was taken out and cooled rapidly with ice bath. Before analysis, the solvent was kept in a sealed container and aged for two weeks. The heated solution was denoted as 150-CU or 210-CU, depending on the temperature during heating.

5. Electrode preparation and Electrochemical tests

All electrochemical data were collected using CHI660e electrochemical workstation (Chenhua, Shanghai) and a LAND battery program-control test system at room temperature (25±5 ^{o}C).

The working electrodes used for Li-ion cell were prepared with a slurry coating technique. The slurry consisted of 80 wt.% active materials, 10 wt.% acetylene black (AB) and 10 wt.% poly(vinylidene fluoride) (PVDF) dissolved in N-methyl pyrrolidinone (NMP), and was then incorporated onto a nickel foam. To prepare electrode for assembling coin type lithium cell, the nickel foam is a round piece with a diameter of 12 mm. To prepare electrode used for supercapacitor, coating area was typically 1 cm × 1 cm. The coating masses are both about 1.0 mg. After being dried at 60 ^{o}C for 24 h, the coated nickel foam were pressed under a pressure of 10 MPa.

To study lithium storage behavior, coin-type cells (CR 2025) were assembled in an argon-filled glovebox with metallic lithium foil as both the reference and counter electrodes. 1 M $LiPF_6$ in ethylene carbonate (EC)-dimetryl carbonate (DME) (1:1 in volume) as the electrolyte, and a polypropylene (PP) microporous film (Cellgard 2300) as the separator. To test the pseudocapacitive performance, a three-electrode electrochemical cell containing 1 M KOH. A Pt plate and Hg/HgO electrode were used as

1 the counter electrode and reference electrode, respectively.

2 To evaluate the electro-catalytic property of the material, a glassy carbon electrode was used. 1 mg
3 active material was first dispersed in 2 mL water. Then 20 μL turbid liquid was transferred to the
4 surface of a glassy carbon electrode (5 mm diameter) by a microsyringe. After drying, the electrode
5 was further coated with 20 μL 0.01 wt.% Nafion aqueous solution, dried and used as working
6 electrode. The test was taken in a three-electrode cell containing an aqueous solution of 0.1 M Na_2CO_3
7 and 0.1 M CH_3OH. A Pt foil was used as counter electrode. A saturated calomel electrode (SCE)
8 immersed in saturated KCl solution and connected with salt bridge was used as reference electrode.
9

Discussion of TG

The TG curves of 10C-S Ni LDH and 50W Ni LDH (Figure S1a and S1b) show that their thermal behavior under Ar can be considered to be two endothermic weight-loss processes (25~150 ^{o}C and 250~400 ^{o}C). The first process (25~150 ^{o}C) should be attributed to the gradual deintercalation of water and other organic species from the interlayer region of LDH. The second process (250~400 ^{o}C) should be attributed to phase transformation caused by cleavage of bonds. It's note worthy that in the second process (250~400 ^{o}C) of TG curve for 10C-S Ni LDH (Figure S1a), the peak in the heat flow curve is split into two peaks compared with that of 50W Ni LDH. This strongly imply that instead of bond cleavage of Ni-O, there might be another kind of atom which is directly bonded to Ni^{2+}.

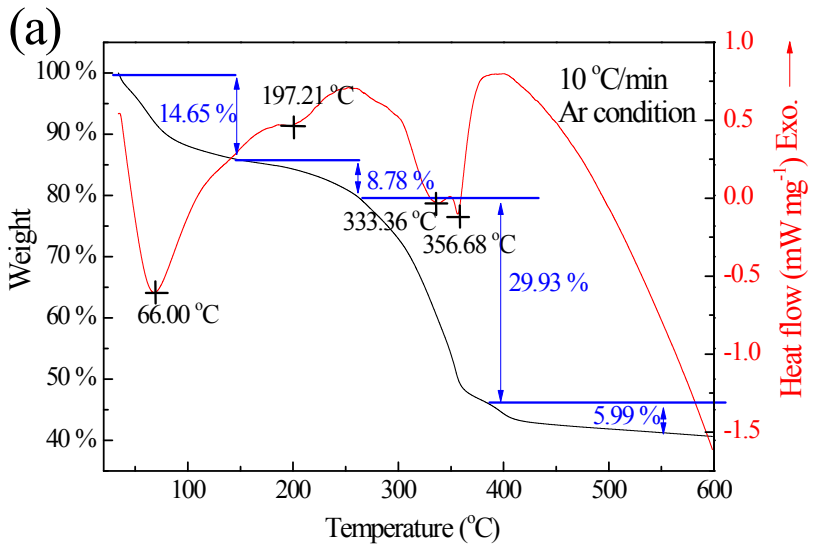

1

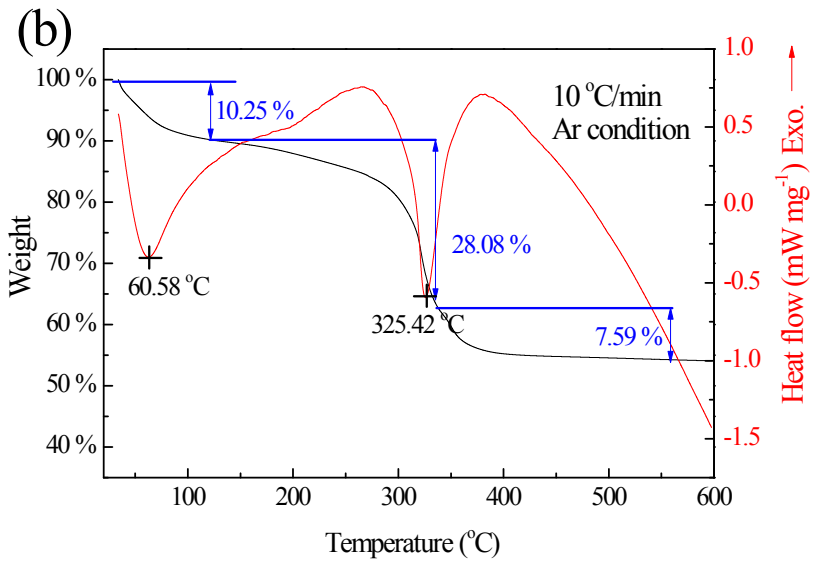

2

3 **Figure S1** TG curves of 10C-S Ni LDH (a) and 50W Ni LDH (b). The experiments were performed

4 under Ar atmosphere. The heating rate is 10 °C/min.

5

UV-Vis, FTIR and XPS

The UV-Vis spectra of 10C-S Ni LDH and 50W Ni LDH are given in Figure S2a. The UV-Vis curve of 50W Ni LDH is very similar with that of layered hydroxide nickel acetate previously reported.[3] For 10C-S Ni LDH, an extra peak at 677 nm can be distinguished, which suggests the existence of different bonding mode of Ni^{2+}.

FTIR is used to identify the functional group of the intercalated species (Figure S2b). The broad band at high wavenumber (3600~3200 cm^{-1}) reflects the intensive hydrogen bonds in the interlayer region of the layered structure, which is also observed for Co LDH.[2b] The FTIR spectra of both 10C-S Ni LDH and 50W Ni LDH have a peak centered at about 2212 cm^{-1}, which corresponds to N=C=O. This peak becomes significantly asymmetric for 10C-S Ni LDH, which shows OCN^- should bond to the nickel layer with various modes.

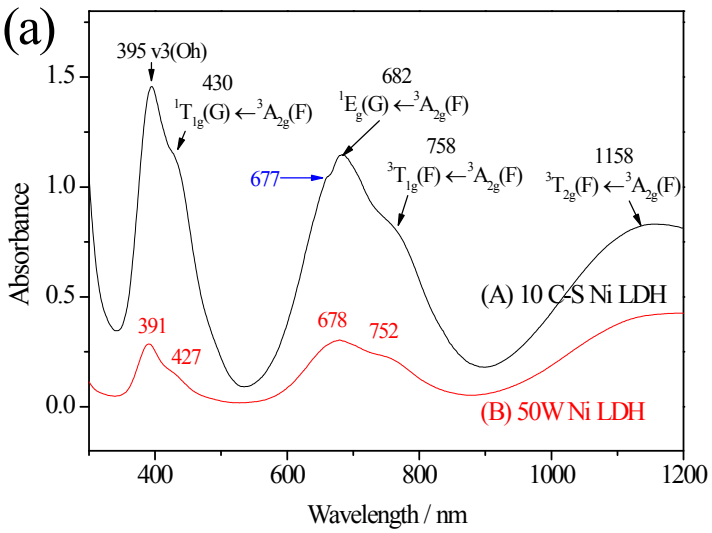

1

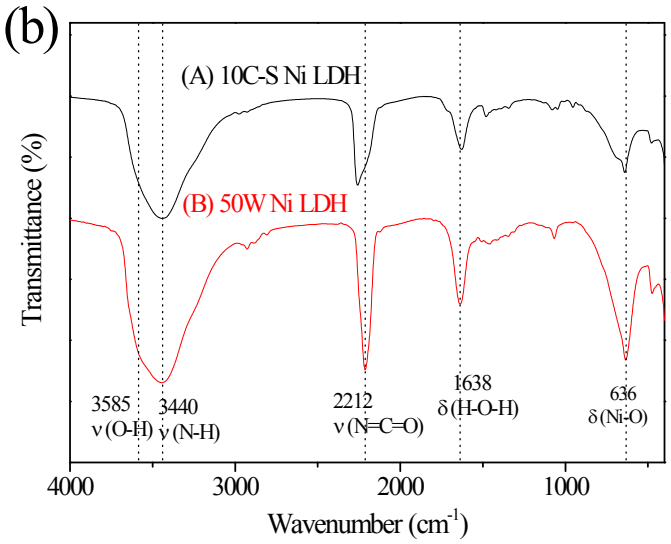

2

3

4 **Figure S2** UV-Vis (a) and FTIR spectra (b) of 10C-S Ni LDH and 50W Ni LDH.

5

6

7

1

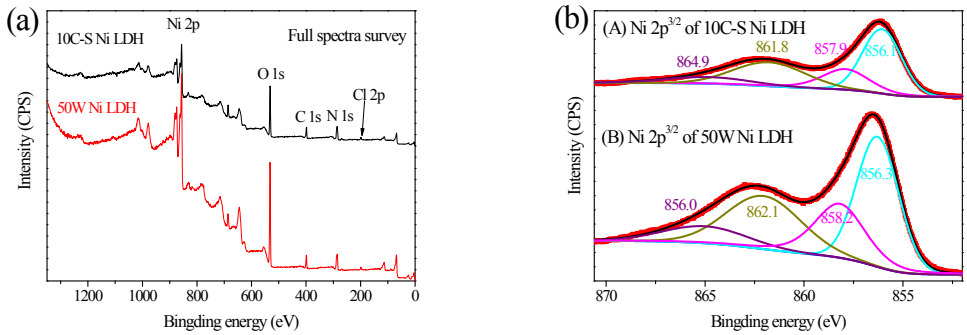

2

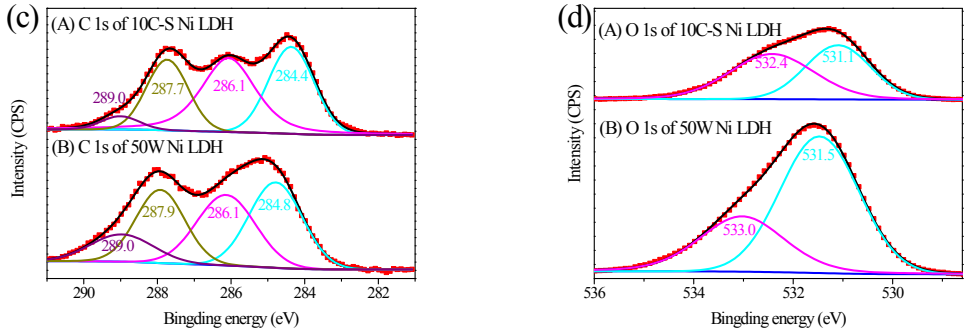

3

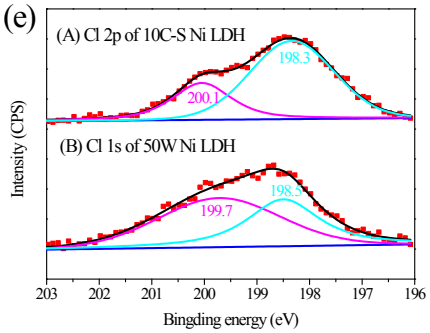

4 **Figure S3** XPS spectra of 10C-S Ni LDH and 50W LDH. (a) gives the full spectra survey. (b-e) gives

5 the deconvolution of individual peaks for Ni, C, O and Cl element.

6

7

Discussion of ^{1}H NMR and FTIR of CU before/after thermal decomposition, and the unique solvent effect.

^{1}H NMR and FTIR study

Figure S4 shows the ^{1}H NMR spectra of CU, 150-CU and 210-CU. The resonance peak at around 3.2 ppm was arbitrarily normalised to 9, corresponding to the nine hydrogen atom in $–CH_3$ of ChCl (see its molecular structure in **Figure S4**). For the pristine CU, the resonance peak at 6.05 ppm is attributed to the $–NH_2$ of urea. The integral value of this peak is 8.4, higher than theoretical value of 8 for a 1ChCl: 2Urea mixture. This might be due to the higher purity of urea than that of ChCl, resulting in a slightly larger urea content. A very broad peak was found at 4.75. This should correspond to the protons from the –OH on ChCl and water.[4]

The NMR spectrum of 150-CU basically preserves the characteristic in that of CU. The area of the peak at 6.05 ppm slightly decreased, indicating the decomposition of small amount of urea. Two peaks emerged at 5.38 and 4.39 ppm , respectively. The peak at 4.39 ppm was also observed previously when heating a CU/water system at 140 ^{o}C for 10 min.[5] It was ascribed to the formation NH_4OH. The peak at 5.38 ppm should correspond to the protons from the –OH on ChCl and water. Note that this heating condition (150 ^{o}C, 40 min, the same as that used to synthesize Ni LDH), where the temperature is much higher than normal urea decomposition threshold of ~90 ^{o}C, only leads to partial decomposition of urea. Because urea has strong interaction with choline chloride through hydrogen

bonding.[5] The decomposition of urea is accompanied with the gradual decrease of polarity.[5] But the supramolecular structure of the CU is not destructed at this stage.

When further heated to 210 ^{o}C, the original peaks corresponding to urea and ChCl are severely broadened (**Figure S4**C). Lots of disordered peaks emerged in the range of 2.5~4.5 ppm, indicating complicated reactions during decomposition. Both urea and ChCl molecules are destructed under this condition.

The thermal decomposition process of CU is further understood with FTIR characterization. The peaks are indexed based on rational analysis in **Figure S5**. The shapes of CU, 150-CU and 210-CU are generally similar. But from CU to 150-CU to 210-CU, several peaks ranging from 1700-1100 cm^{-1} (marked by red in **Figure S5**) become weaker and obviously broadened. As these peaks correspond to $–NH_2$ (1685 and 1615), $-CH_3$, and –CN, it implies that thermal decomposition of urea and choline chloride is accompanied with the cleavage of bonds around nitrogen atoms, and subsequent formation of other complex molecules including cyanate salts.

Solvent effect

OCN^- plays an important role in triggering the self-reduction process. However, since strong signal for N=C=O is also detected by FTIR in 50W Ni LDH, the insertion of OCN^- should be a necessary but not sufficient condition for achieving self-reduction. The bonding mode is also very important. Bora and coworkers synthesized Ni LDH by heating an aqueous solution of Ni^{2+} and urea.[6] Samples were

withdrawn at different reaction time. Through in-depth bonding analysis based on FTIR and XPS, it's found that the bonds in cyanate species exhibit different geometries in Ni LDH. With increasing time, cyanate changed from N-bonded to O-bonded end-on geometries. This was explained by the different driving force from steric and/or electronic contributions. It's proposed that steric requirements for an angular M-OCN (M for metal) linkage would be greater than that for a linear M-NCS bonding. On the other hand, O-bonded cyanate mode donates more electrons although energetically less stable. At beginning, steric factors prevent cyanate from coordinating through oxygen. Later, electronic factors dominate and favor either oxygen or bridging coordinations.[6]

The unique self-reduction phenomenon can thus be understood if the solvent effect provides different steric factors and electronic factors compared with that of aqueous solution. The solvent used in this work is a ChCl/urea (CU) type deep eutectic solvent (DES). DESs are a relatively new class of ionic liquids (ILs). ILs are liquids composed of ions and thus having unusual physiochemical properties compared with water or traditional organic solvents. Liquid CU forms by mixing solid urea and choline chloride. The main driving force is the formation of intensive hydrogen bonds.[1, 7] Previous molecular dynamic simulation and theoretical study indicate that with hydrogen bond interaction urea inserts into the ChCl lattice, and the chloride ion is dislocated.[8] The CU possess a supramolecular structure and is highly polar.[9] The supramolecular structure should make the steric factor more significant, thus hindering the formation of Ni-O bond. However, thermal decomposition would

gradual destruct the supramolecular structure. The decomposition process of CU is too complex to be precisely characterized. Kurt and coworkers used GC-MS to investigate the electrochemical decomposition process of a choline chloride/ethylene glycol type DES. A range of chlorinated products like chloromethane, dichloromethane and chloroform could be detected, as well as other species like 2-methyl-1,3-dioxolane.[10] Ana and coworkers performed ^{1}H NMR for CU heated at 140 ^{o}C for different time.[5] Under this condition, the urea portion decomposed gradually. The polarity of the solvent decreased. But the ChCl/urea substantial supramolecular integrity wasn't affected by partial urea decomposition.

The ^{1}H NMR and FTIR results indicate that under the condition for synthesizing the Ni LDHs, the functional group and supramolecular structure can basically preserve. The decomposition of choline chloride portion in CU is not severe (see ^{1}H NMR and FTIR spectra of 150-CU in Figure S1 and S2). But if higher temperature is used, the supramolecular structure would be severely destructed (see ^{1}H NMR and FTIR spectra of 210-CU in Figure S1 and S2). In our previous work to synthesize Co LDH based on a similar "hot-injection" technique, it's also found that the structure of products synthesized at 150 ^{o}C and 210 ^{o}C are very different.[2b] These results indicate the properties of CU, including those affect the steric factors, are very dynamic during heating and sensitive to the experimental condition. Under a suitable circumstance, the CU solvent can favor the steric factors that hinders the formation of Ni-O bonds and provide better kinetics for the formation of Ni-N bonds.

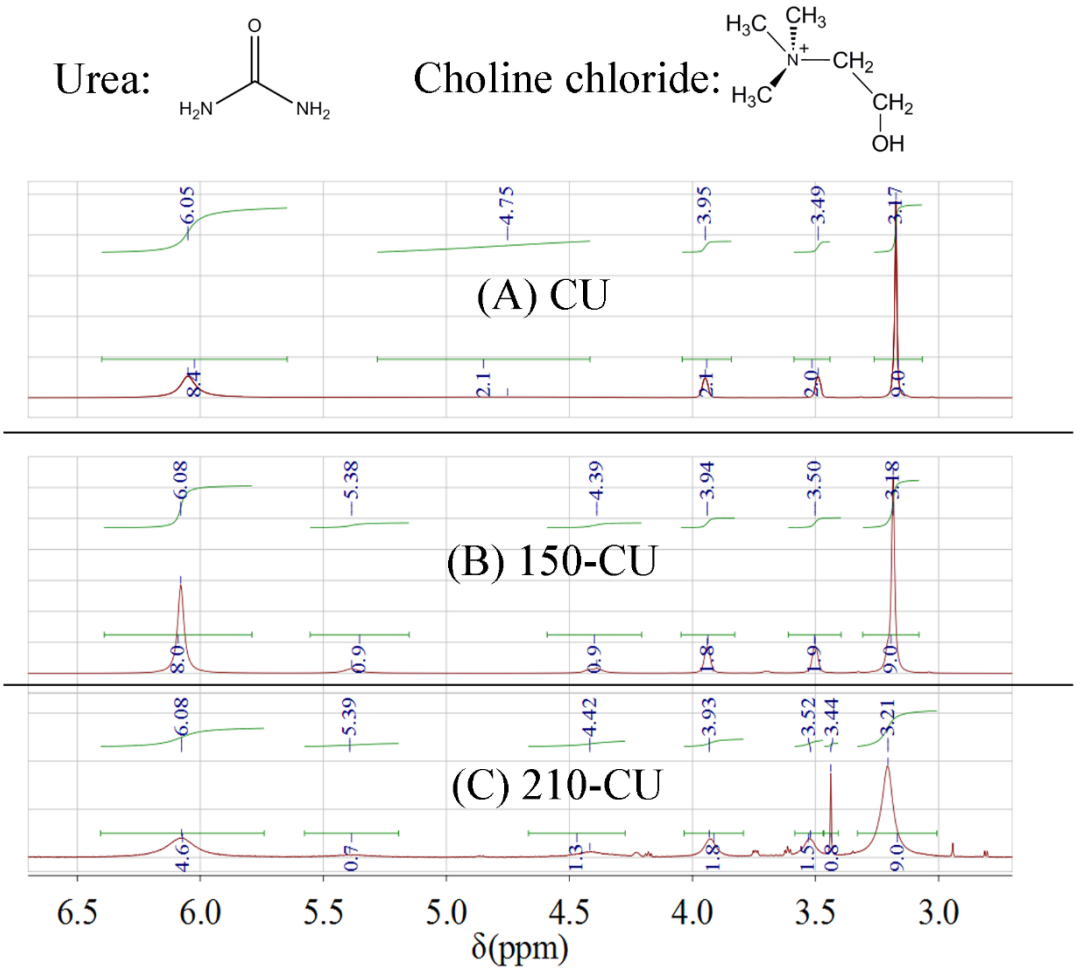

Figure S4 ^{1}H NMR spectra of CU, 150-CU and 210-CU. The peak positions and their integrals are indicated on top and bottom, respectively. The molecular structures of choline chloride and urea are also given at the top of the figure.

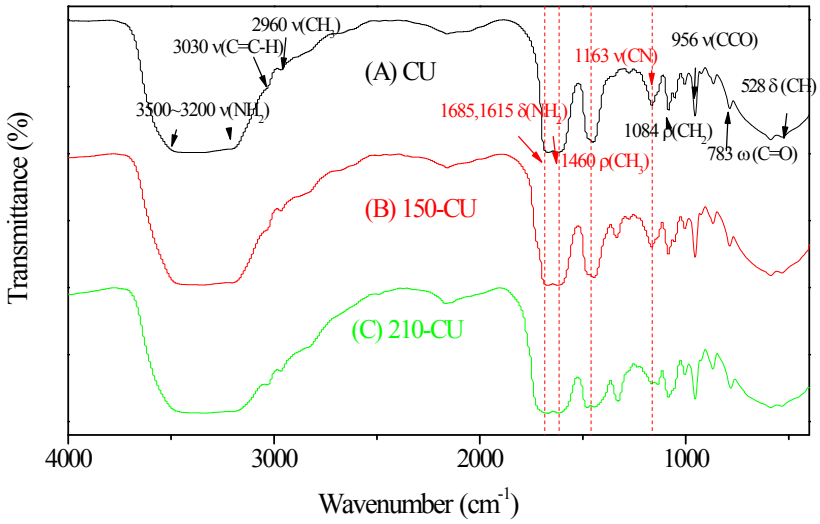

1

2 **Figure S5 FTIR** spectra **of CU, 150-CU and 210-CU.**

Enhanced performance in various electrochemical application and kinetic study Electrochemical performance

NiO has been intensively studied as functional material due to its easy availability and cost effectiveness. Previously, we fabricated NiO mesoporous nanoflower by annealing Ni LDH in air.[2a, 11] The obtained mesoporous NiO showed better electrochemical performance as active material in electrocatalysis and supercatacitor than flower-like NiO reported by other researchers.[12] Its advantage benefits from the flower like morphology with ultra small size (~100 nm), focused size distribution and small grain size.[2a, 11] However, NiO is commonly an n-type semiconductor with very low conductivity. Merely optimizing morphology can hardly solve this problem. Previously, Huang and coworkers demonstrate that introducing Ni could greatly improve the performance of NiO in Li-ion cell.[13] Figure S6 shows that the HCP Ni introduced by self-reduction can have a general improvement for NiO in several important electrochemical applications, including electro-catalysis, supercapacitor and Li-ion battery.

The **electro-catalysis** for methanol using NiO is a promising technique for direct methanol fuel cell (DMFC). It's reported that NiO show better catalytic behavior in carbonate electrolytes.[14] The 10C-S A-Ni and 50W A-Ni samples were dispersed on glassy carbon electrode and cycled in aqueous electrolyte containing 0.1 M Na_2CO_3 and 0.1 M CH_3OH. The cycling performance was evaluated by monitoring the current density at 0.7 V (vs. SCE) when the electrodes were repeatedly cycled between

0.2 V and 1 V (vs. SCE) at scan rate of 0.01 V s^{-1} (Figure S6a). The current density for 10C-S A-Ni is 25.8 A g^{-1} at the first cycle and gradually decays to 1.6 A g^{-1} after fifty cycles, better than 50W A-Ni (from 16.1 to 1.1 A g^{-1}). These values are higher than those tested for mesoporous NiO nanoflower in KOH electrolyte (about 1.1 A g^{-1} during chronoamperometric test at 0.7 V vs. SCE).[11] CV tests are performed for 10C-S A-Ni (Figure S7a) and 50W A-Ni (Figure S7b) with or without methanol. For both materials, when cycled in 0.1 M Na_2CO_3 without methanol, a pair of redox peaks show at 0.5 V and 0.65 V (vs. SCE) respectively. In the presence of methanol, the current densities gradually arise with the potential (Figure7S). These features are similar with NiO/CNT tested in KOH electrolyte,[15] thus indicating the catalytic mechanism of 10C-S A-Ni in Na_2CO_3 electrolyte should be similar with what's previously proposed.[11] NiO converts to NiOOH in alkaline solution during anodic scan and then NiOOH can react with CH_3OH to achieve catalytic oxidation.[15]

Supercapacitor has emerged as a promising device for electrochemical energy storage.[16] NiO is a promising candidate for pseudocapacitors for its cost effectiveness, good pseudocapacitive behavior and easy availability.[17] Figure S6b gives the pseudocapacitive cycling stability of 10C-S A-Ni and 50W A-Ni at a high current density of 10 A g^{-1}. The capacitance is derived using $C = I\Delta t/M\Delta V$ based on chronopotentiometry curves (Figure S8), where C (F g-1) is the specific capacitance. I (mA) represents discharge current. M (mg), ΔV (V) and Δt (s) mean the mass of active material, potential range during discharge and total discharge time, respectively.[2c] After 4000 cycles, 10C-S A-Ni still

has a high capacitance of 706 F g^{-1}, obviously higher than that of 50W A-Ni (576 F g^{-1}). Both 10C-S A-NI and 50W A-Ni show better pseudocapacitive performance than those flower-like NiO with size at micrometer scales reported by other researchers.[12, 18]

Lithium ion battery has long been considered an attractive power source for a wide variety of applications. Nano sized transition metal oxides can store a large amount of Li^+ through conversion mechanism.[19] Previously, Huang and coworkers demonstrate that the introduction of Ni into NiO can improve its performance in Li-ion system.[13] It's proposed nano sized Ni can improve the coulombic efficiency and cycling performance due to its catalytic activity to decompose Li_2O and SEI film.[13] Figure S6c gives the cycling stability of both 10C-S A-Ni and 50W A-Ni at current rate of 300 mA g^{-1}. 10C-S A-Ni can retain a specific capacity of 593.7 mAh g^{-1}, higher than 369.7 mAh g^{-1} for 50W A-Ni. For comparison, Mai and coworkers reported that NiO nanoflake arrays directly grown on Ni foam delivers 463.3 mAh g^{-1} specific capacitity at the 50^{th} cycle tested at 100 mA g^{-1}.[20] If doped with cobalt, the Co-doped NiO has a specific capacitance of 589.5 mAh g-1 at the 50^{th} cycle tested at 100 mA g^{-1}.[20] The improvement was attributed to the improved conductivity because the n-type NiO was converted to a p-type semiconductor with higher conductivity. These results clearly indicate that improving conductivity is a powerful method for optimizing NiO electrode, which is achieved by embedding HCP Ni in this work.

Electrochemical kinetics study

To reveal the improved electrochemical kinetics of 10C-S A-Ni compared with 50W A-Ni, they were taken for further kinetic analysis in Li-ion system. Because Li-ion cell suffer from the least self-discharge, thus being more stable at equilibrium state than electrocatalytic or pseudocapacitive systems which use aqueous electrolyte. The different voltage between charge and discharge process, also called voltage hysteresis, is a main problem for materials based on conversion mechanism. Figure S9a gives the voltage hysteresis curves obtained by subtracting the discharge curve at the second cycle from the charge curve at the first cycle after normalization.[21] For the normalization used in Figure S9a, 0 refers to full delithiated state when charged to 3.0 V and 1.0 refers to lithiated state. Both 10C-S A-Ni and 50W A-Ni show lower hysteresis under gradual lithiation due to enhanced electronic conductivity when NiO converts to Li_2O and Ni. This phenomenon is also observed for other transition metal oxide like NiO and Co_3O_4.[2b, 21] 10C-S A-Ni has a lower hysteresis at the lithiated state (normalized capacity > 0.6) but higher hysteresis at the delithiated state (normalized capacity < 0.4). It doesn't show obvious overall difference (Figure S9a) in its hysteresis behavior though much larger specific capacity (Figure S9c).

Electrochemical impedance spectroscopy (EIS) and galvanostatic intermittent titration technique (GITT) techniques can combine transient and steady-state measurements.[22] They were successfully used together to understand the electrochemical kinetic for other transition mental metal oxides like

MnO,[23] Co_3O_4,[2b] or hybrid material like Fe_3O_4/SWNT[22] NiO/rGO and MnO_2/rGO.[21, 24] Figure S9b gives the Nyquist plots. The Z' and Z'' values have been multiplies with the mass of active materials. The Nyquist plots of 10C-S A-Ni and 50W A-Ni both consist of a depressed semicircle and a long low-frequency line. The high-frequency region for 10C-S A-Ni and 50W A-Ni almost overlaps with each other. But 10C-S A-Ni has smaller resistance in medium and low frequency region. These results indicate that the two materials have similar kinetics for fast process (Li-ion traveling through SEI layer) but different kinetics for processes with moderate (charge transfer resistance, R_{ct}) and slow (diffusion related Warburg impedance) speed. The EIS spectra can be approximately fitted using a modified Voigt-type equivalent circuit (Figure S9c).[2b] Levi previously developed an equivalent circuit analogue based on a combination of a Voigt-type analogue and generalized Frumkin and Melik-Gaukazyan impedance to simulate the impedance of Li-ion inserting into carbon electrode.[25] The feature is that it consists of several R||C in series to model the Li-ion migration through SEI film with multilayer structure evidenced by Aurbach and coworkers with XPS.[26] Considering the conversion mechanism and porosity of the A-Ni materials, we used a constant phase element (CPE) to replace the pure capacitor in parallel with R_{ct} and eliminate the C_{int} which was used to represent insertion capacitance of graphite electrode in Levi's model.[25] This modified Voigt-type equivalent circuit has been successfully applied to simulate mesoporous Co_3O_4 nanosheets in our previous work.[2b] The calculated impedance based (lines in Figure S9b) on this circuit is in acceptable accordance to the measured

impedance data (dots in Figure S9a). However, the electrochemical reaction involves formation and decomposition of complex intermediate phases. Nickel and oxygen atoms (ions) also move. It's difficult to derive accurate kinetic parameters with unambiguous physiochemical significance. We only quantatively conclude that 10C-S A-Ni and 50W A-Ni have similar impedance when Li-ion migrate through multilayer SEI films. But electron transfer resistance and diffusion impedance for 10C-S A-Ni is obviously smaller.

Figure S9d and S9f display GITT curves for 10C-S A-Ni and 50W A-Ni, respectively. The difference between the cutoff potential and the open-circuit potential after relaxation can be used to roughly reflect polarization.[2b] For 50W A-Ni, the polarization slightly decreases with lithium insertion and increases during lithium extraction (Figure S9f). From the view of conductivity, metallic state nickel forms during lithium insertion and can increase conductivity. This trend is less obvious for 10C-S A-Ni (Figure S9d). Because the existence of HCP Ni already enhances the conductivity of 10C-S A-Ni. The shorter distance of cutoff potential and relaxed potential for 10C-S A-Ni (distance in vertical coordinate between the dot line and the solid line in Figure S9d) than 50W A-Ni (Figure S9f) also imply the enhanced conductivity. The GITT potential-time profiles at third discharge pulse (Figure S9e for 10C-S A-Ni and Figure S9g for 50W A-Ni) are used to investigate staggering hysteresis in voltage. 10C-S A-Ni has slightly smaller overpotential (0.31 V, Figure S9e) than that of 50W A-Ni (0.33 V, Figure S9g). The GITT discharge process of both electrodes have two different regions (A

and B). In region A, the potential exhibits a linear relationship with the square root of titration time (inset of Figure S9e and S9g), which indicates a diffusion-controlled process. Though it can not be determined whether it's the diffusion of nickel or oxygen that contributes most. For 50W A-Ni, the potential-time relationship is linear (Figure S9g). Such kind of linear polarization has been explained as strain accommodation energy of phase transformation for $LiFePO_4$ electrode.[27] But for region B of 10C-S A-Ni, the potential decreases with time with some instability (Figure S9e). This can be understood by considering the more complex boundary structure between HCP Ni and NiO as observed by TEM (Figure 2b). The polarization contributed by region B for 10C-S A-Ni is smaller (~0.10 V, Figure S9e) than that for 50W A-Ni (~0.17 V, Figure S9g). It implies the introduction of HCP Ni, or the introduction of boundary phase could alleviate the strain during phase transformation.

1

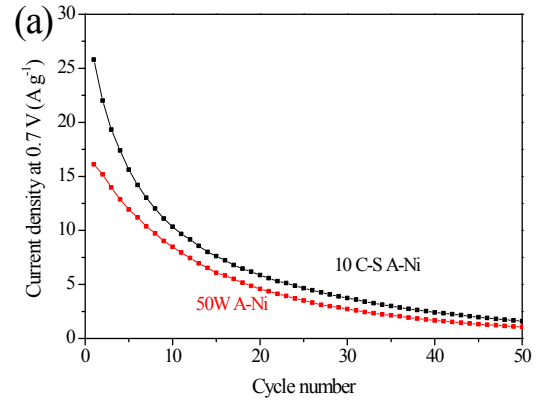

2

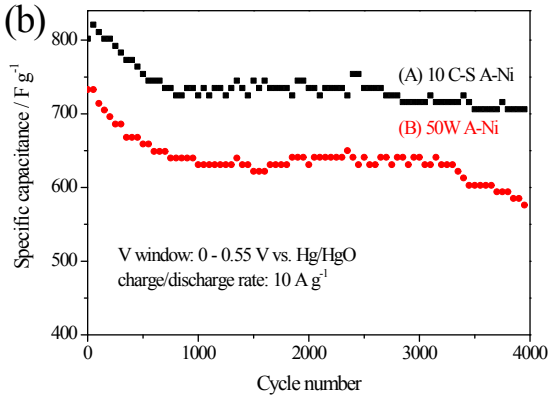

3

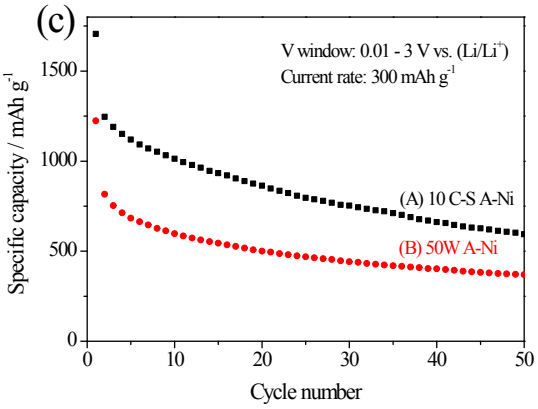

4 **Figure S6** General improved performance of 10C-S A-Ni in various electrochemical applications

5 compared with that of 50W A-Ni. (a) is the cycling performance used in electrocatalysis for methanol

6 at 0.7 V vs. SCE. (b) is the cycling performance used in supercapacitor at charge/discharge rate of 10A

7 g^{-1}. (c) is the cycling performance used in Li-ion cell at charge/discharge rate of 300 mA g^{-1}.

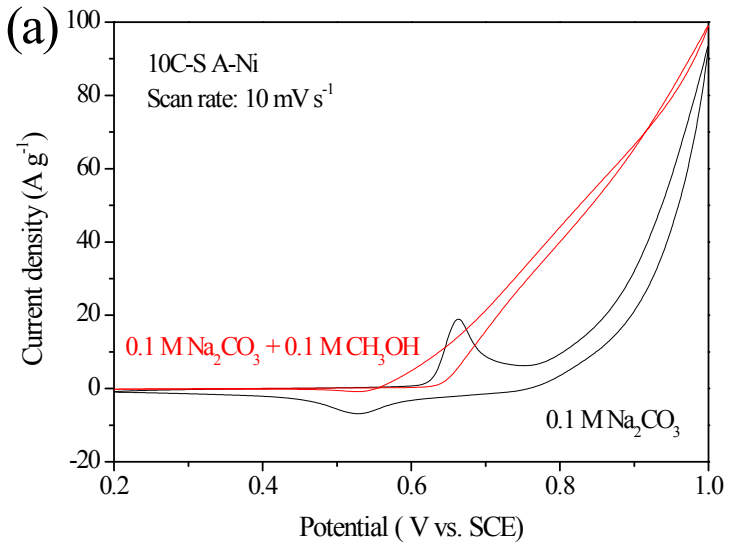

1

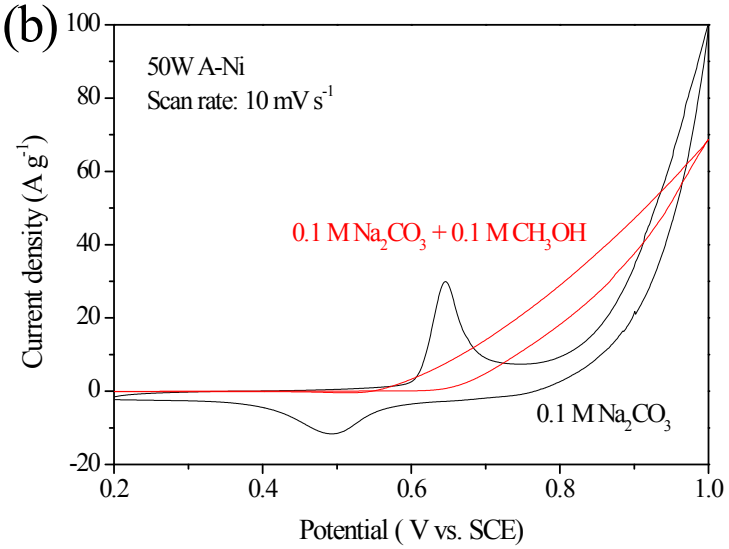

2

3 **Figure S7** 3rd CV cycle at scan rate of 10 mV s^{-1} for glassy carbon electrode modified by (a) 10C-S A-

4 Ni and (b) 50W A-Ni. The electrolytes are 0.1 M Na_2CO_3 solution with or without methanol.

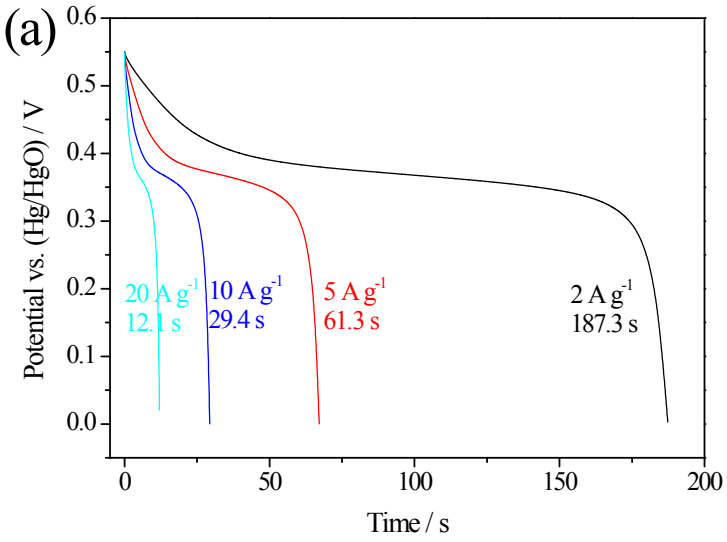

1

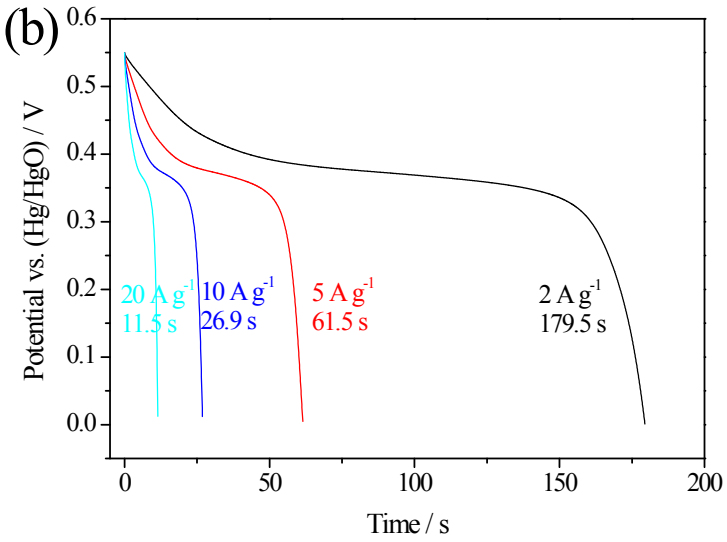

2

3 **Figure S8** Chronopotentiometry curve in supercapacitor (a) 10C-S A-Ni (b) 50W A-Ni

4

5

6

7

1

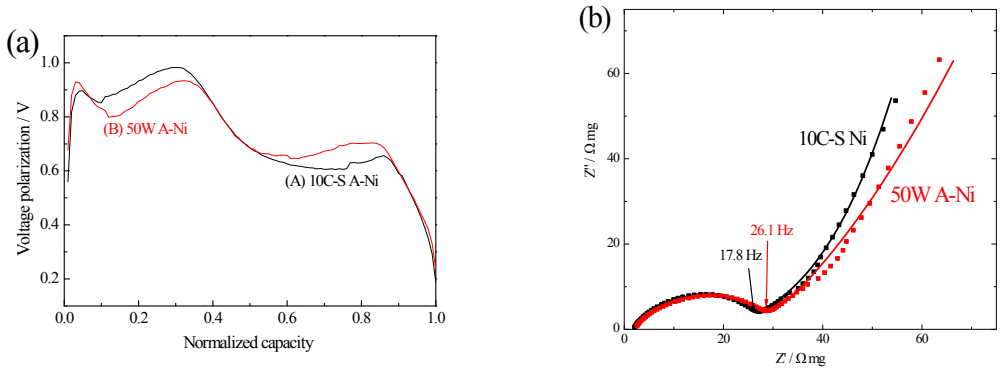

2

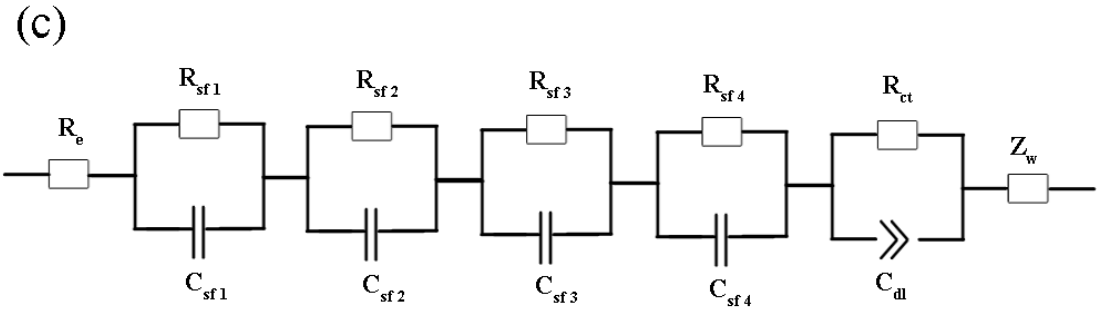

3

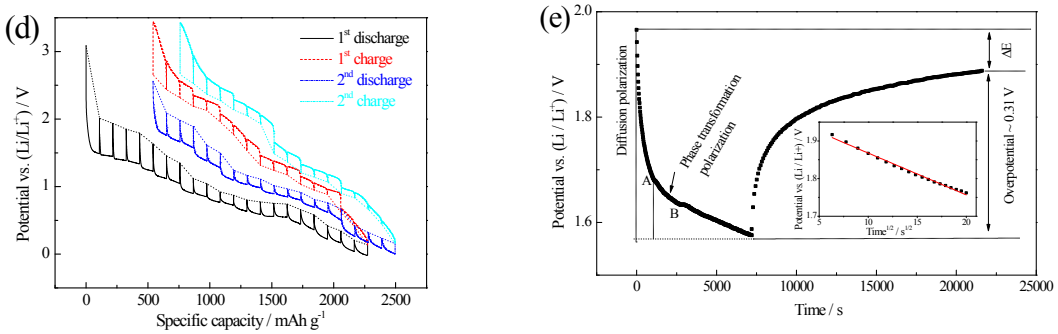

4

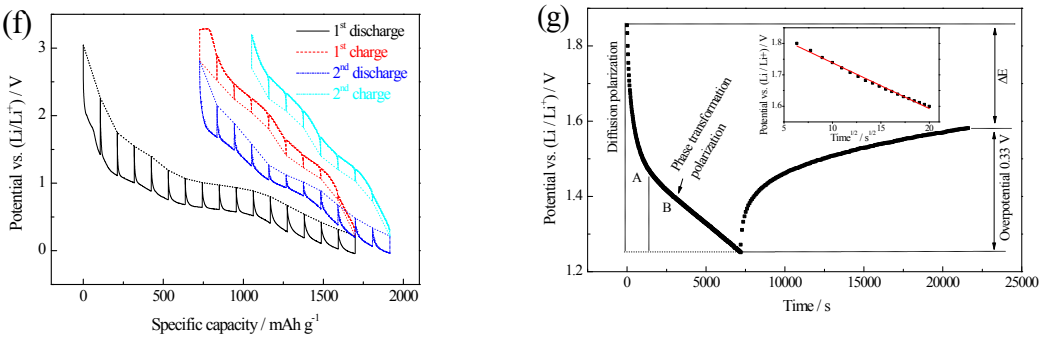

5 **Figure S9** Electrochemical dynamic analysis of 10C-S A-Ni and 50W A-Ni used in Li-ion cell system.

6 (a) shows the voltage polarization at 300 mA g^{-1}. (b) gives the Nyquist plots, where the presented Z'

and Z'' data have been multiplied with the mass of active materials. (c) is the proposed equivalent circuit for simulation. (d) and (f) are the GITT test of 10C-S A-Ni and 50W A-Ni obtained by charging/discharging the cells for 2h at 50 mA g^{-1} and relaxed for 4h in each pulse, respectively. (e) and (g) are the potential-time profile of GITT curve at the third discharge current pulse in the 2^{nd} cycle for 10C-S A-Ni and 50W A-Ni, respectively. ΔE stands for voltage change in pseudoequilibrium before and after current pulse.

Elemental stoichimometry of the Ni LDH samples are analysed by ICP-AES, IC and CNH elemental analyser. Given amount of samples (See **Table S1**) are used to obtain a solution containing H_2SO_4. For IC and ICP-AES experiments, the above solution are diluted by 100 times with deionized water. Based on the original data provided in **Table S1-S4**, the ratio of element in each sample is calculated and given in **Table S5**. The nominal chemical formulars of 10C-S Ni LDH, and 50W Ni LDH are determind to be **$NiC_{1.290}O_{2.907}N_{0.770}H_{3.884}Cl_{0.144}$, and $NiC_{0.893}O_{2.723}N_{0.449}H_{2.742}Cl_{0.055}$, respectively.**

IC, ICP-AES and CNH analysis

Table S1 Mass of samples dissolved for IC and ICP-AES analysis

	Mass / mg	solution
10C-S LDH	**5.23**	2.55 mL 0.78% H_2SO_4
50W Ni LDH	**4.97**	

Table S2 C,N,H elemental analysis results

	N %	C %	H %
10C-S LDH	7.64	11.04	2.79
50W Ni LDH	5.08	8.65	2.23

Table S3 IC analysis, the samples in Table S1 are **diluted by 100 times**

	Cl^- (mg L^{-1})	**Original Cl^- mass ration**
10C-S LDH	0.728	**3.55 %**
50W Ni LDH	0.299	**1.53 %**

Table S4 ICP-AES analysis, the samples in Tables S1 are **diluted by 100 times.**

	Ni (mg L^{-1})	**Mass ratio in the sample (Ni)**
10C-S LDH	8.58	**41.8 %**
50W Ni LDH	9.23	**47.4 %**

Table S5 elemental stoichiometry

	Atomic weight ratio	Atomic molar ratio
10C-S Ni LDH	$Ni_{0.4183}C_{0.1104}O_{0.3315}N_{0.0764}H_{0.0279}Cl_{0.0355}$	$NiC_{1.290}O_{2.907}N_{0.770}H_{3.884}Cl_{0.144}$
50W Ni LDH	$Ni_{0.4736}C_{0.0865}O_{0.3515}N_{0.0508}H_{0.0223}Cl_{0.0153}$	$NiC_{0.893}O_{2.723}N_{0.449}H_{2.742}Cl_{0.055}$

References

1 A. P. Abbott, G. Capper, D. L. Davies, R. K. Rasheed and V. Tambyrajah, *Chem. Commun.*, 2003, 70.

2 (a) X. Ge, C. D. Gu, Y. Lu, X. L. Wang and J. P. Tu, *J. Mater. Chem. A*, 2013, **1**, 13454; (b) X. Ge, C. D. Gu, X. L. Wang and J. P. Tu, *J. Phys. Chem. C*, 2013, **118**, 911; (c) *J. Mater. Chem. A*, 2014, **2**, 17066.

3 L. Poul, N. Jouini and F. Fiévet, *Chem. Mater.*, 2000, **12**, 3123.

4 M. a. C. Gutiérrez, M. L. Ferrer, C. R. Mateo and F. del Monte, *Langmuir*, 2009, **25**, 5509.

5 A. Querejeta-Fernández, J. C. Hernández-Garrido, H. Yang, Y. Zhou, A. Varela, M. Parras, J. J. Calvino-Gámez, J. M. González-Calbet, P. F. Green and N. A. Kotov, *ACS Nano*, 2012, **6**, 3800.

6 B. Mavis and M. Akinc, *Chem. Mater.*, 2006, **18**, 5317.

7 M. Francisco, A. van den Bruinhorst and M. C. Kroon, *Angew. Chem. Int. Ed.*, 2013, **52**, 3074.

8 (a) S. L. Perkins, P. Painter and C. M. Colina, *J. Phys. Chem. B*, 2013, **117**, 10250; (b) H. Sun, Y. Li, X. Wu and G. Li, *J. Mol. Model.*, 2013, **19**, 2433.

9 (a) A. Pandey, R. Rai, M. Pal and S. Pandey, *PCCP*, 2013, **16**, 1559; (b) E. R. Parnham, E. A. Drylie, P. S. Wheatley, A. M. Slawin and R. E. Morris, *Angew. Chem.*, 2006, **118**, 5084.

10 K. Haerens, E. Matthijs, K. Binnemans and B. Van der Bruggen, *Green Chemistry*, 2009, **11**, 1357.

11 C. D. Gu, M. L. Huang, X. Ge, H. Zheng, X. L. Wang and J. P. Tu, *Int. J. Hydrogen Energy*, 2014, **39**, 10892.

12 (a) Y. Ren and L. Gao, *J. Am. Ceram. Soc.*, 2010, **93**, 3560; (b) Q. Wu, Y. Liu and Z. Hu, *J. Solid State Electrochem.*, 2013, **17**, 1711.

13 X. Huang, J. Tu, B. Zhang, C. Zhang, Y. Li, Y. Yuan and H. Wu, *J. Power Sources*, 2006, **161**, 541.

14 N. Spinner and W. E. Mustain, *Electrochim. Acta*, 2011, **56**, 5656.

15 X. Tong, Y. Qin, X. Guo, O. Moutanabbir, X. Ao, E. Pippel, L. Zhang and M. Knez, *Small*, 2012, **8**, 3390.

16 X. Xia, D. Chao, Z. Fan, C. Guan, X. Cao, H. Zhang and H. J. Fan, *Nano Lett.*, 2014, **14**, 1651.

17 X.-h. Xia, J.-p. Tu, X.-l. Wang, C.-d. Gu and X.-b. Zhao, *J. Mater. Chem.*, 2011, **21**, 671.

18 H. Chai, X. Chen, D. Jia, S. Bao and W. Zhou, *Mater. Res. Bull.*, 2012, **47**, 3947.

19 P. Poizot, S. Laruelle, S. Grugeon, L. Dupont and J. Tarascon, *Nature*, 2000, **407**, 496.

20 Y. Mai, J. Tu, X. Xia, C. Gu and X. Wang, *J. Power Sources*, 2011, **196**, 6388.

21 Y. Mai, S. Shi, D. Zhang, Y. Lu, C. Gu and J. Tu, *J. Power Sources*, 2012, **204**, 155.

22 Z. Cao and B. Wei, *ACS Appl. Mater. Interfaces*, 2013, **5**, 10246.

23 K. Zhong, B. Zhang, S. Luo, W. Wen, H. Li, X. Huang and L. Chen, *J. Power Sources*, 2011, **196**, 6802.

24 Y. Mai, D. Zhang, Y. Qiao, C. Gu, X. Wang and J. Tu, *J. Power Sources*, 2012, **216**, 201.

25 M. Levi and D. Aurbach, *J. Phys. Chem. B*, 1997, **101**, 4630.
26 D. Aurbach, I. Weissman, A. Schechter and H. Cohen, *Langmuir*, 1996, **12**, 3991.
27 Y. Zhu and C. Wang, *J. Power Sources*, 2011, **196**, 1442.